Future ocean acidification in the Canada Basin and surrounding Arctic Ocean from CMIP5 earth system models

N. S. Steiner,[1] J. R. Christian,[1] K. D. Six,[2] A. Yamamoto,[3] and M. Yamamoto-Kawai[4]

[1] Six Earth system models that include an interactive carbon cycle and have contributed results to the 5th Coupled Model Intercomparison Project (CMIP5) are evaluated with respect to Arctic Ocean acidification. Projections under Representative Concentration Pathways (RCPs) 8.5 and 4.5 consistently show reductions in the bidecadal mean surface pH from about 8.1 in 1986–2005 to 7.7/7.9 by 2066–2085 in the Canada Basin, closely linked to reductions in the calcium carbonate saturation state $\Omega_{A,C}$ from about 1.4 (2.0) to 0.7 (1.0) for aragonite (calcite) for RCP8.5. The large but opposite effects of dilution and biological drawdown of DIC and dilution of alkalinity lead to a small seasonal amplitude change in Ω, as well as intermodel differences in the timing and sign of the summer minimum. The Canada Basin shows a characteristic layering in Ω: affected by ice melt and inflowing Pacific water, shallow undersaturated layers form at the surface and subsurface, creating a shallow saturation horizon which expands from the surface downward. This is in addition to the globally observed deep saturation horizon which is continuously expanding upward with increasing CO_2 uptake. The Eurasian Basin becomes undersaturated much later than the rest of the Arctic. These CMIP5 model results strengthen earlier findings, although large intermodel differences remain: Below 200 m Ω_A varies by up to 1.0 in the Canada Basin and the deep saturation horizon varies from 2000 to 4000 m among the models. Differences of projected acidification changes are primarily related to sea ice retreat and responses of wind mixing and stratification.

1. Introduction

[2] As carbon dioxide (CO_2) dissolves in seawater, it forms carbonic acid (H_2CO_3) which dissociates to release hydrogen ions (H^+) ("ocean acidification"). This decreases the concentration of carbonate (CO_3^{2-}) ions and thus the saturation state of seawater with respect to aragonite and calcite, the two forms of calcium carbonate ($CaCO_3$) commonly produced by marine organisms. The saturation concentration is roughly 1.5 times higher for aragonite than for calcite as is dictated by the solubilities of the two minerals.

[1]Fisheries and Oceans Canada, Institute of Ocean Sciences and Canadian Centre for Climate Modelling and Analysis, Sidney, British Columbia, Canada.

[2]Department of The Ocean and The Earth System, Max Planck Institute for Meteorology, Hamburg, Germany.

[3]Division of Climate System Research, University of Tokyo, Chiba, Japan.

[4]Department of Ocean Sciences, Tokyo University of Marine Science and Technology, Tokyo, Japan.

Corresponding author: N. S. Steiner, Fisheries and Oceans Canada, Institute of Ocean Sciences and Canadian Centre for Climate Modelling and Analysis, PO Box 6000, 9860 West Saanich Rd., Sidney, BC V8L 4B2, Canada. (Nadja.Steiner@ec.gc.ca)

Hence, aragonite is more vulnerable to undersaturation (saturation state Ω below 1.0) under increasing ocean acidification. When freshwater inputs with zero total alkalinity (TA) and dissolved inorganic carbon (DIC) dilute the affected water masses and consequently decrease the partial pressure of CO_2 (pCO_2) in the ocean, the resulting disequilibrium between ocean and atmosphere leads to increased CO_2 uptake which further decreases pH and Ω. With nonzero concentrations of DIC and/or TA in river water [e.g., *Tank et al.*, 2012] or accumulated DIC released with meltwater [e.g., *Loose et al.*, 2009], this effect would be reduced [*Cai et al.*, 2010, Figure 4.]. Diluted seawater exhibits a greater decrease in pH with added CO_2 and reaches undersaturation of $CaCO_3$ sooner. The models largely ignore fluvial DIC and TA, or use a global mean concentration. However, the effect of nonzero concentrations of DIC and TA on Ω_A is small as long as the ratio of DIC to TA in river water is similar to seawater [*Tank et al.*, 2012]. Since the solubility of CO_2 in sea water increases with decreasing temperatures, cold Arctic waters have naturally low saturation states for aragonite and calcite (Ω_A and Ω_C) and are especially vulnerable to further decline due to the combined effects of increased atmospheric CO_2 and increased freshwater inflow from river runoff and ice melt, as well as localized upwelling of acidic waters [*Yamamoto-Kawai et al.*, 2009; *Chierici and Fransson*,

2009; *Yamamoto-Kawai et al.*, 2011; *Carmack and McLaughlin*, 2011]. While enhanced primary production can seasonally increase the saturation state, subsequent remineralization of sinking material reduces the saturation state in the subsurface. Earlier climate model projections based on the SRES scenarios [*Nakicenovic et al.*, 2000] have suggested continued reductions in saturation states [e.g., *Orr et al.*, 2005; *Steinacher et al.*, 2009; *Denman et al.*, 2011] for the entire Arctic. A model study by *Yamamoto et al.* [2012] points out the importance of the rate of loss of sea ice on acidification, suggesting that future reductions in pH and aragonite saturation states could be significantly faster than previously projected with an increased rate of sea ice reduction.

[3] Observations of biogeochemical variables in the Arctic are generally sparse and seasonally biased. There are few time series studies of ocean chemistry in the Arctic. The JOIS (Joint Ocean Ice Study) program in the Canada Basin (CB), and Barrow Strait, Nares Strait, and Davis Strait monitoring lines are among the few such programs. The C3O (Canada's 3 Oceans) program, covering transects through the Bering Strait, the CB and the Canadian Arctic Archipelago (CAA) added a one-time base line study. L. Miller et al. (Changes in the marine carbonate system of the Western Arctic: Patterns in a rescued data set, submitted to *Polar Research*, 2013) consolidated several decades of inorganic carbon measurements in a consistent data set. They as well as earlier publications by *Yamamoto-Kawai et al.* [2009] and *Chierici and Fransson* [2009] report aragonite undersaturation in surface and shallow subsurface waters of the CB, Beaufort Sea and CAA.

[4] From an Earth system model (ESM) perspective, the CAA is not well or not at all resolved and shallow coastal seas are difficult to properly represent in coarse resolution models. Hence, the CB presents itself as a reasonable test bed for ESM intermodel comparisons supported by observations. The individual ESMs show little spatial change with respect to saturation state in the central CB ($\approx$ 74–82°N,130–150°W) and results from a representative grid point coinciding either with a long-term oceanic station (75°N, 140°W) or coinciding with the greatest model depth within the CB (77.5°N, 136°W) are presented in this study.

[5] Acidification can significantly affect growth, metabolism, and life cycles of marine organisms [*Gattuso and Hansson*, 2011, and references therein] and hence has received increased attention both within the scientific community and from stakeholders. An assessment of Arctic Ocean Acidification was recently completed by the Arctic Monitoring and Assessment Program [*AMAP*, 2013]. The 5th Coupled Model Intercomparison Project [CMIP5, *Taylor et al.*, 2012] includes for the first time a variety of ESMs, allowing the study of future projections of the marine carbon cycle. In this study, we evaluate the current state and future projections of aragonite and calcite saturation states in the Arctic based on results from six ESMs submitted to CMIP5 (Table 1). All models use the same atmospheric greenhouse gas concentrations. They differ in horizontal resolution and bathymetry, affecting in and outflow of the Arctic Basin as well as throughflow (e.g., through CAA) and mixing processes (e.g., on the shelves), and parameterizations within their individual modules (see Table 1 and references therein).

[6] Retreating sea ice is one of the main components leading to increased acidification of the Arctic Ocean, both due to the addition of melt water and due to the increase in open water areas allowing for enhanced air-sea exchange. The latter leads to a more pronounced seasonality in atmosphere-ocean carbon fluxes with a delayed maximum in uptake in fall and an explicit minimum in uptake or even outgassing in July and August [*Steiner et al.*, 2013]. *Stroeve et al.* [2012] find that while CMIP5 models better capture the observed decline in Arctic sea ice than earlier models [*Stroeve et al.*, 2005], the newer models exhibit a stronger seasonal cycle in both sea ice extent, and volume and the intermodel scatter remains large, particularly in summer. It is also noted that the spatial pattern of ice thickness is not simulated well by the majority of models [*Maslowski et al.*, 2012; *Stroeve et al.*, 2012].

[7] Evaluating ESMs for biogeochemical variables with much lower data availability is even more problematic. In recent years, the development of biogeochemical components in ESMs has advanced significantly from the first generation of ESMs with interactive carbon cycles [e.g., *Friedlingstein et al.*, 2006; *Denman et al.*, 2007]. However, the still fairly coarse horizontal (0.3–2°) and vertical (10–50 m) resolution restricts the ability to resolve biological or chemical processes in the euphotic zone as well as small-scale physical processes important for biogeochemistry.

Table 1. Description of Ocean-Ecosystem Components of ESMs[a] Used in This Study and Timing of Surface Undersaturation in the Annual Mean for Simulations With RCPs 4.5 and 8.5 in the Central Canada Basin (136°W,77.5°N)

Model	Dimensions[b] Ocean: x-y-z	Ecosystem[c]	References	$\Omega_A < 1$ Timing[c] RCP8.5	$\Omega_A < 1$ Timing[d] RCP4.5
HadGEM2-ES	360×216×40	N3P2ZD	*HadGEM2 Development Team* [2011], *Collins et al.* [2011]	2010–2014	2014
MIROC-ESM	256×192×44	NPZD	*Watanabe et al.* [2011], *Kawamiya et al.* [2000]	2015–2020	2016
MPI-ESM-LR	256×220×40	N3PZD	*Giorgetta et al.* [2013], *Ilyina et al.* [2013]	2015–2027	2015–2027
CanESM2	256×192×40	NPZD	*Arora et al.* [2011], *Christian et al.* [2010]	2020	2025–2027
GFDL-ESM2M	360×200×50	N4P3D	*Dunne et al.* [2012, 2013]	2037–2049	2037–2063
IPSL-CM5A-LR	182×149×31	N5P2Z2D	*Dufresne et al.* [2013], *Aumont et al.* [2003]	2040–2042	2044–2049

[a]A more elaborate table can be found in *Vancoppenolle et al.* [2013].

[b]Number of grid points in the horizontal (x, y) and vertical (z), reflecting horizontal resolutions ranging from 0.3–1° to a maximum of 2°.

[c]Ecosystem complexities are indicated via numbers of nutrient (N), phytoplankton (P), zooplankton (Z), and detritus (D) groups.

[d]Timing when surface Ω_A falls below one. For some models, a range is provided, indicating a time of first occurence and a time when Ω_A remains below one. If only 1 year is given, Ω_A remains below one after first occurrence.

Hence, while ESMs simulate global spatial and seasonal patterns with fair accuracy, model skill for biogeochemical variables in global ESMs is still low [e.g., *Schneider et al.*, 2008; *Steinacher et al.*, 2010]. This is especially true for the Arctic, where data are few and seasonally biased, and shelf areas and narrow passages are common features. Nonetheless, the ability of ESMs to provide an estimate of changes in response to rising atmospheric CO_2 and other greenhouse gas levels and climate warming makes them an important tool in addressing consequences for socioeconomic activities. Multimodel ensemble (MME) means and model scatter can provide a general trend and an indication of uncertainty of the simulated results. Often multimodel ensembles are used as a more reliable measure of future change. However, emergent features in MMEs should be viewed with caution. They may be spurious and can arise because of common errors in a particular MME or because of overly influential models [*Bracegirdle and Stephenson*, 2013]. This study presents an analysis of projected Arctic Ocean acidification in CMIP5 ESMs. In the following sections, we describe the models and methods (section 2), present results (section 3), and provide a discussion (section 4), and summary (section 5).

2. Methods

[8] The ESMs included in this study are: CanESM2, GFDL-ESM2M, HadGEM2-ES, IPSL-CM5A-LR, MIROC-ESM, and MPI-ESM-LR. These are the first six models which provided the required biogeochemistry fields (see below), as well as sea-ice cover, that were made available via the CMIP5 data portal (http://cmip-pcmdi.llnl.gov/cmip5/data_portal.html). They provide a good representation of the available Earth System Models, and later submissions have not been included in the analysis. Additional fields of surface pH and Z_m (monthly maximum ocean mixed layer thickness defined by each model's mixing scheme) are not available for all models (no pH for MIROC-ESM, no Z_m for MIROC-ESM and HadGEM2-ES). A limited description of the models is provided in Table 1 and more details can be found in references provided therein. Apart from the slightly varying resolutions (Table 1), it is worth noting that the CAA throughflow is represented either via crude openings for Parry Channel and Nares Strait (GFDL-ESM2M, HadGEM2-ES), Nares Strait only (MPI-ESM-LR, MIROC-ESM, IPSL-CM5A-LR) or unresolved and approximated via diffusive mixing between Baffin Bay and the Beaufort Sea (CanESM2). The marine ecosystem is represented either via single representations of nutrient (N), phytoplankton (P), zooplankton (Z), and detritus (D) groups (NPZD, for CanESM2 and MIROC-ESM); via enhanced representations including two to three limiting nutrients and one or two phytoplankton groups (MPI-ESM, HadGEM2-ES); or via multiple representatives of all groups, adding up to >20 tracers (GFDL-ESM2M, IPSL-CM5A). The state of the ocean carbon system was calculated offline from 3-D fields of DIC, TA, temperature (T), and salinity (S) in order to maintain consistency across models. All calculations were performed according to the Best Practices Guide of *Dickson et al.* [2007] using the equilibrium constants of *Lueker et al.* [2000]. Saturation states were calculated using the expressions for mineral solubility of *Mucci* [1983] with the

pressure correction of *Millero* [1979]. Constant reference concentrations were applied for phosphate, silicate, and calcium. DIC and TA in sea ice and sea ice melt water are zero for all models. For most models DIC and TA inputs from rivers are also neglected (CanESM2, MIROC-ESM, MPI-ESM-LR, HadGEM2). In those models sediment deposition of TA is compensated by a globally uniform weathering flux. GFDL-ESM2M and IPSL-CM5A-LR do include fluvial DIC and TA, but use a global mean concentration that is probably too low for the Arctic.

[9] The experiments analyzed in this study include simulations for the historical 1850–2005 period and for the future 2006–2100 period using the Representative Concentration Pathways 8.5 (no mitigation) and RCP4.5 (with mitigation) [*Moss et al.*, 2010]. Data were regridded to a uniform $2° \times 2°$ grid for all models via distance-weighted average remapping of the four nearest neighbor values using Climate Data Operators (http://www.mad.zmaw.de/Pingo/post/post.cdo.home.html). Model variables are shown as time series or means for bidecadal time periods from 1966–1985 to 2066–2085.

3. Results

3.1. Comparison to Observations

[10] For the Arctic, no gridded data sets of carbon chemistry are available. Hence, comparisons to observations are limited to temporal and spatial snapshots obtained from irregular research cruises and programs of finite duration. Figure 1a shows surface Ω_A calculated from observed DIC and TA for the time period 1986–2005 as summarized via the CARINA Data Synthesis Project (http://cdiac.ornl.gov/oceans/CARINA). The poor spatial coverage is apparent; nonetheless, the data indicate consistently low saturation states (0.7–1.3) in the Beaufort Sea/western CB and higher saturation states in the Eurasian Basin (1.7) and North Atlantic (1.7–2.3). Reduced saturation states can also be found along the Greenland coast in the Arctic outflow regions. *Steinacher et al.* [2009] and *Yamamoto-Kawai et al.* [2009] report from available observations that the aragonite saturation state in the CB decreased from about 1.3 in 1997 to 0.8–1.1 in 2008. Extensions into the CAA show large variability in saturation states. *Chierici and Fransson* [2009] find values between 1.3 and 4.9 for Ω_C and 0.8–3.1 for Ω_A during a transect in 2007. They attribute hot spots of low saturation to varying contributions of sea ice melt, river inflow, upwelling of CO_2 enriched subsurface water and enhanced organic matter remineralization, and they link very high saturation states to intense biological production. Recently, compiled data from the Western Arctic show substantial changes since the 1970s and averaged observations from the Beaufort Sea (BS) and CB, show the mean Ω_A at the surface still supersaturated (i.e., >1), but upper halocline waters and deep waters now show regularly occurring aragonite undersaturation (Miller et al., submitted manuscript, 2013). *Yamamoto-Kawai et al.* [2011] calculate decreases in aragonite saturation state of 0.2 in 1997 and 0.6 in 2008, relative to preindustrial values. Figure 1b shows a cross section of Ω_A estimated from observations of DIC and TA along the 140°W transect (70–78°N) during the cruise of the Joint Ocean Ice Study (JOIS) in August 2011. The observations show surface
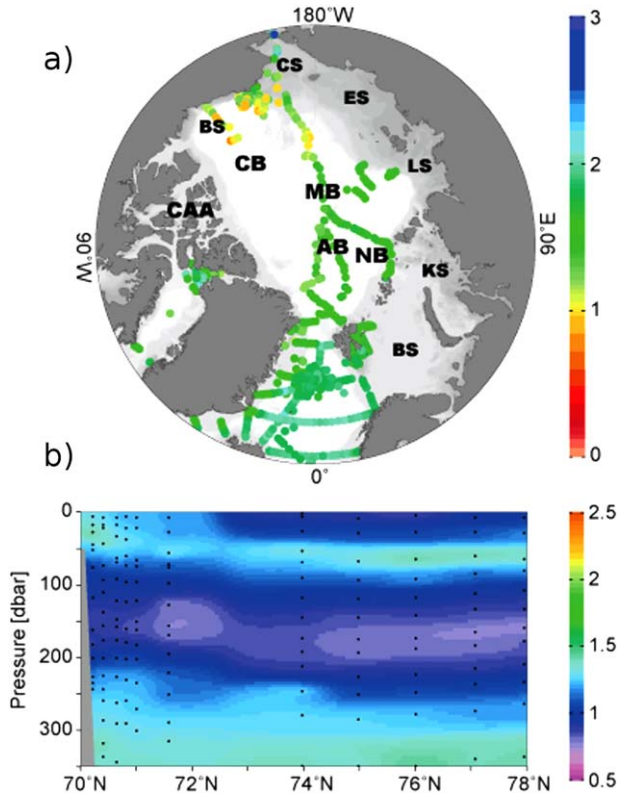
Figure 1. (a) Surface aragonite saturation Ω_A for the time period 1986–2005 as summarized via the CARINA Data Synthesis Project and (b) observed aragonite saturation Ω_A for August 2011 along the 140°W JOIS transect from 70 to 78°N. The ice edge is located at approximately 71.5°N at the time (derived from ice charts, http://www.ec.gc.ca/glaces-ice/). (Area indicators in Figure 1a) are CAA: Canadian Arctic Archipelago, CB: Canada Basin, BS: Beaufort Sea, CS: Chuckchi Sea, ES: Eastsiberian Sea, LS: Laptev Sea, KS: Kara Sea, BS: Barents Sea, MB: Makarov Basin, AB: Amundsen Basin, NB: Nansen Basin).

waters close to the coast still supersaturated, but a shallow layer of undersaturated waters crossing the central Beaufort gyre where sea ice disappears in summer (although at the time of the transect, the area north of 71.5°N was still mostly ice covered). At depths, between about 20 and 100 m, waters are still supersaturated due to advection of Summer Pacific Water and to photosynthesis at the subsurface Chl-a maximum. A band of undersaturated waters is seen below the deep halocline (100–200 m). This subsurface undersaturated layer is maintained by advection of Pacific Winter Water (PWW) which is characterized by high nutrient concentrations and high pCO_2 due to remineralization of organic matter as the water flows over the shallow Chukchi shelf during winter. Below PWW is Atlantic Water with high Ω, which flows into the intermediate layer of the CB [see also *Yamamoto-Kawai et al.*, 2009; *Bates and Mathis*, 2009]. An indication of this layered structure can also be seen in the observations presented in *Steinacher et al.* [2009] for a transect north of the CB. A similar feature implying that surface waters might become undersaturated with respect to aragonite while the underlying water is still saturated was also reported for the Southern Ocean

(Weddell Sea) [*Hauck et al.*, 2010]. A comparison with the ESM simulations is challenging due to the snapshot character of the observations and the fact that only annual data are available for 3-D ocean biogeochemistry fields. Figure 2 shows the model representations of the expanded JOIS transect along 140°W for the 2006–2025 bidecadal average (model output extend from 70–88°N). All models show a reduction in upper ocean Ω_A compared to the 1986–2005 average (not shown), with undersaturated surface waters in most models (CanESM2, HadGEM2-ES, MPI-ESM-LR, MIROC-ESM). Interestingly, a structure similar to that in the 2011 observations is only seen in CanESM2 and to a limited extent in HadGEM2-ES. The latter prominently displays a lens of undersaturated surface waters (as observed) but does not show the supersaturated subsurface layer extending from the coast toward the North Pole. While this feature in CanESM2 is consistent with the observations it is likely due to an excessive shelf depth (190 m in Can-ESM2 compared with a more realistic 25–50 m in the other models), which inhibits complete mixing on the shelves. As a consequence, CanESM2 simulates a layered structure in the Chukchi Sea which is also persistent in the CB.

[11] Figure 3 shows the modeled bidecadal annual mean profiles of T, S, DIC, nTA (TA referenced to S = 35 ppt), and Ω_A for 2006–2025 and 2066–2085 at 75°N, 140°W and the projected temporal evolution of the multimodel mean from 1986–2005 to 2066–2085 for DIC, nTA, and Ω_A. Black lines and triangles in Figures 3a–3c, 3f, and 3i show observed profiles to 350 m at the same location for summer 2005. Again, the snapshot character of the observations severely limits the comparison. While the simulated profiles are generally in a similar range, the observed profiles show a layered near surface structure in T and Ω_A which cannot be seen in the bidecadal model average. While this might be due to the temporally limited character of the observations, a large part is likely due to a limited ability of the models to resolve the characteristic vertical structure in the CB. The simulated profiles show a large intermodel spread which has already been pointed out for other biogeochemical fields [*Vancoppenolle et al.*, 2013], suggesting the main value of these ESMs to be in the projected change rather than the absolute value. Future projections of these profiles will be discussed below.

3.2. Projections in the Canada Basin

[12] Figure 4 and Table 2 show the multimodel comparison of bidecadal averages for annual mean surface pH, Z_m in March and sea ice concentration in March and September. Figure 4 also shows annual Ω_A. Data are spatially averaged for the CB (≈68–79°N, 124–160°W, which for the purpose of this study includes the Beaufort Sea) for the historical and RCP8.5 experiments; results for RCP4.5 are listed in Table 2. The CB domain varies slightly for the various models depending on resolution and landmask. The modeled annual mean pH decreases from 8.12 in 1986–2005 to 7.87 in 2026–2045 and further to 7.77 in 2066–2085 for RCP8.5. For RCP4.5 pH reaches 7.9 by 2066–2085, about 25 years after a respective projection for RCP8.5. The models show a consistent decline with a low intermodel standard deviation of 0.02 (Figure 4a and Table 2). The decrease in pH is closely tracked by a decrease in Ω_A from 1.38 to 0.72 over the same time period
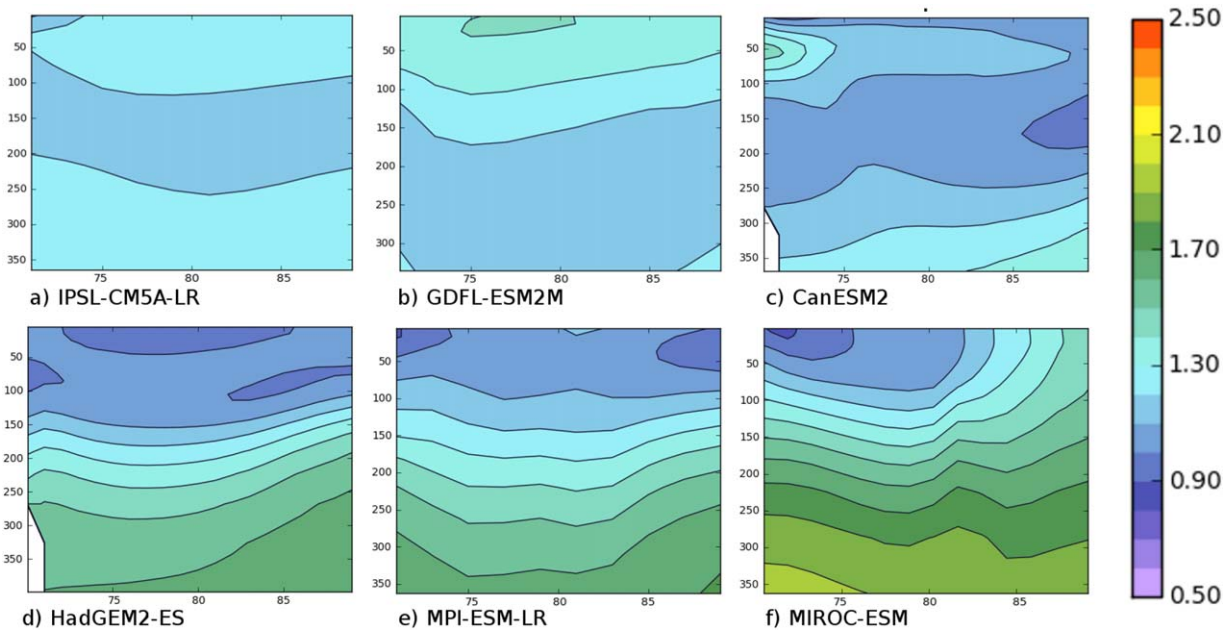
Figure 2. Cross section along the JOIS transect (140°W, 70–88°N) of aragonite saturation state Ω_A as simulated for the RCP8.5 scenario for the bidecadal average 2006–2025: (a) IPSL-CM5A-LR, (b) GFDL-ESM2M, (c) CanESM2, (d) HadGEM2-ES, (e) MPI-ESM-LR, and (f) MIROC-ESM. The section from 70 to 78°N is comparable to the observations shown in Figure1b. Vertical axis shows depth in meters, horizontal axis location in degrees N.

(Figure 4b). Table 2 also provides averages for the Arctic domain covering all ocean grid cells north of 64°N. For pH, the projected decline is only slightly different (Table 2).). Differences are more obvious for Z_m. In the CB domain, the mean Z_m in March decreases from 51 m in 1986–2005 to 48.8 m in 2066–2085 for both RCP 8.5 and 4.5. In the Arctic domain, Z_m decreases from a mean of 83.6 m in 1986–2005 to 71.9 m (77.4 m) in 2066–2085 for RCP 8.5 (4.5), which includes areas of deeper mixing in the northern North Atlantic. The standard deviation of Z_m across models declines from about ±10 to ±5 m in the CB and from about ±18 to ±13 m for the Arctic region, likely representing more uniform mixing in the absence of sea ice for all models. The September multimodel mean sea ice concentration reduces from 45.6% to 0.4% (RCP8.5) and to 9.6% (RCP4.5) in the CB, and from 51% to 3.6% (RCP8.5) and to 15.7% (RCP4.5) for the Arctic region. Variability is high among models, with standard deviations up to 17% (Table 2), however, the reduction to negligible ice cover in September by 2066–2085 in the RCP8.5 scenario is consistent across all models. (for discussions on sea ice concentration in CMIP5 models see *Stroeve et al*. [2012]). While simulated pH and summer ice cover continuously decrease, Z_m in the CB decreases only in the first part of the century and exhibits a less clear signal after, possibly affected by regional inconsistencies (see below).

[13] Of particular interest is the relationship between simulated annual mean pH, March Z_m and September sea-ice cover in the CB for the individual models discussed here. Highest pH and Ω_A are consistently simulated by GFDL-ESM2M which also shows the deepest mixed layers (Figure 4, red symbols). Lowest pH is consistently simulated by MPI-ESM-LR, which also shows shallowest Z_m by

mid/end-century. Sea ice concentrations in MPI-ESM-LR are close to the multimodel mean (Figure 4, light blue symbols). This might suggest a link between the models' representation and progression of ocean acidification and their different patterns of summer sea-ice cover and stratification. However, it needs to be pointed out that Ω_A at 50–100 m depth is not consistently lower or higher than at the surface for the bidecadal means (e.g., Figure 2). Hence in some models, deeper mixing might bring more saturated water to the surface, in others less saturated water. For profiles shown in Figure 3, the upper 150 m represent Pacific influenced water masses, while the intermediate layer below 150–200 m is influenced by Atlantic water. As for 2006–2025 (section 3.1), some intermodel differences are obvious. These differences are to a large part retained in the projection runs, e.g., the prominent low salinity and high nTA signal in the surface ocean of HadGEM2-ES and the low DIC/high Ω_A in the intermediate waters in MIROC-ESM.

[14] In an attempt to attribute some of the changes to model specific biogeochemical parameterizations, Figure 5 shows the annual (ANN) and summer (JJA) mean downward flux of $CaCO_3$ at 100 m depth (i.e., export of biogenic $CaCO_3$). Model specific parameterizations for calcification lead to low export of $CaCO_3$ in the Arctic for all but GFDL-ESM2M and MPI-ESM-LR, which show significant net calcification in the summer months. GFDL-ESM2M shows a decreasing trend in the future projections, which is due to an explicit functional dependence of calcification on acidification, while MPI-ESM-LR shows a fairly strong increase due to enhanced primary production. Calcification removes alkalinity at the surface and increases alkalinity in the subsurface and explains reduction in the nTA difference
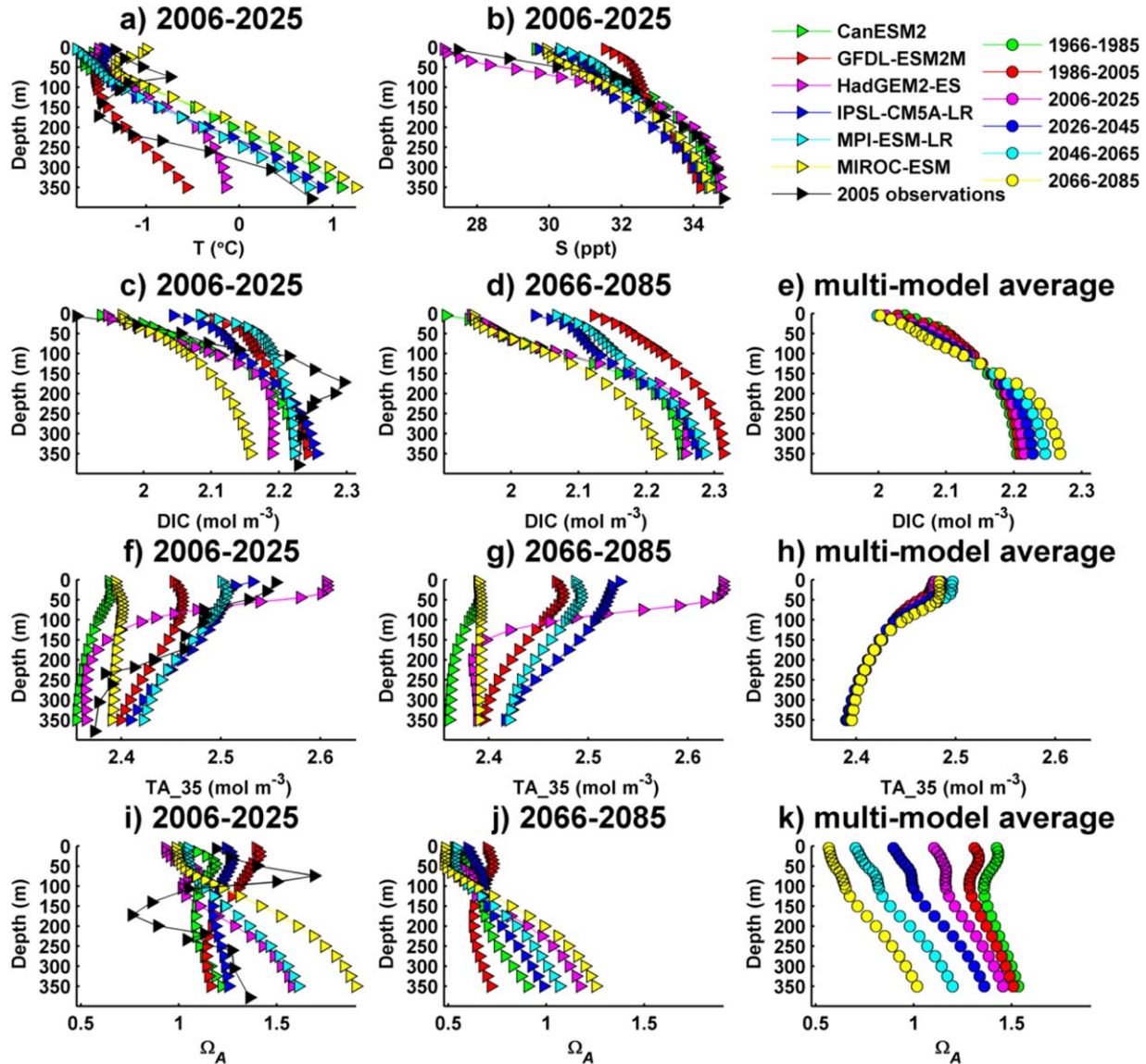
Figure 3. Modeled bidecadal annual mean profiles at 75°N, 140°W of temperature T (°C), salinity S (ppt), dissolved inorganic carbon DIC (mol m^3), total alkalinity normalized to S = 35 ppt nTA (mol m^{-3}), and aragonite saturation state Ω_A for 2006–2025: (a) T, (b) S, (c) DIC, (f) nTA, and (i) Ω_A and 2066–2085: (d) DIC, (g) nTA, and (j) Ω_A. Observations from summer 2005 are overplotted in black for the 2006–2025 time period. Figures 3e, 3h, and 3k show the projected temporal evolution of the multi-model mean from 1986–2005 to 2066–2085 for DIC, nTA, and Ω_A.

between GFDL-ESM2M (red) and MPI-ESM-LR (blue) in the upper 150 m from 2006–2025 to 2066–2085 (Figures 3f and 3g). The larger differences between the models cannot be explained by calcification. The profiles also do not support a grouping of the model results by ecosystem complexity, e.g., there is no consistent difference or lack thereof between NPZD models (CanESM2, MIROC-ESM) and models with multiple functional groups. HadGEM2-ES remains a clear outlier with a large nTA gradient between the surface and 150 m (Figures 3f and 3g). The multimodel mean DIC profile (Figure 3e) shows a slow decrease for the Pacific water influenced upper layers as a consequence of dilution in Arctic near surface waters. In the Atlantic influenced intermediate layers, the multimodel mean trend fol-lows the global increase of DIC in the ocean which is advected into the Arctic from the Atlantic. The multimodel mean change in alkalinity follows the salinity signal and hence the normalized nTA (Figure 3h) shows little change. The acidification trend becomes most obvious in the multimodel mean Ω_A profiles (Figure 3k) which show a continuous reduction in saturation state with surface waters becoming undersaturated by 2026–2045 and full aragonite undersaturation to 350 m by 2066–2085. The multimodel mean also shows the layered structure in the near surface waters of the CB slowly disappearing and developing into a more linear profile with increasing Ω_A from the surface to 350 m. Respective profiles of the basin average are very similar and are omitted.
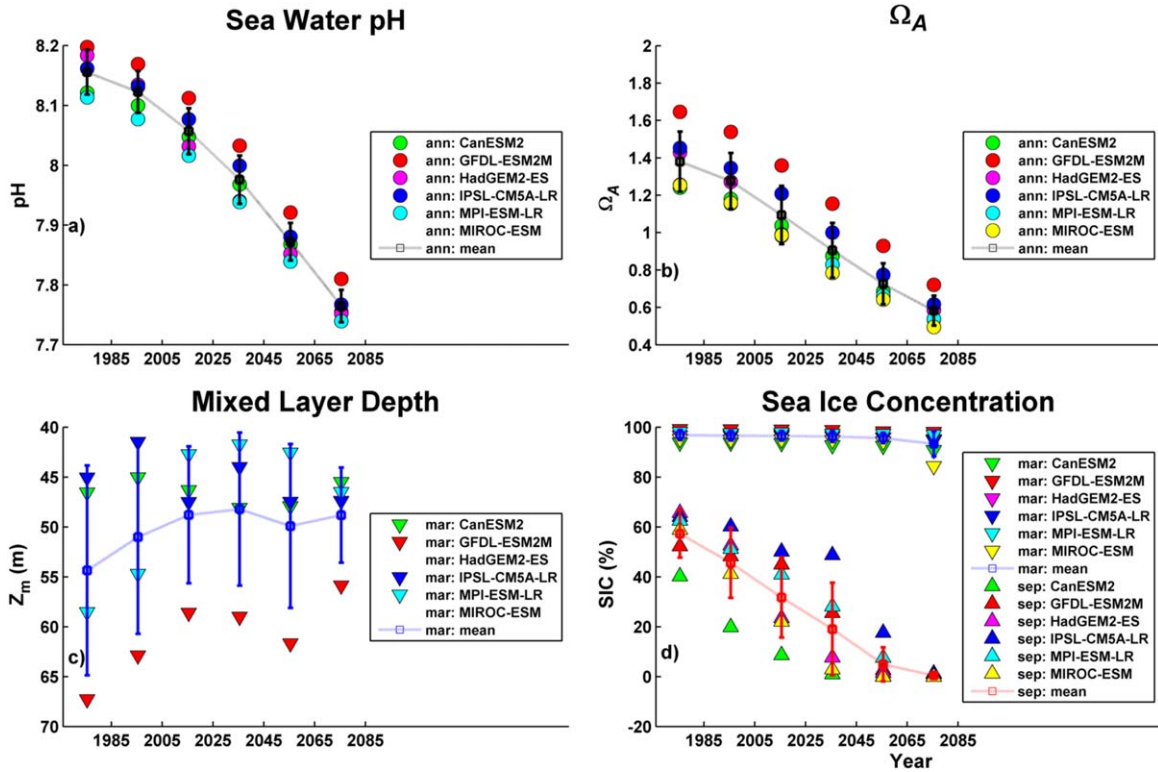
Figure 4. Multimodel comparison of bidecadal averages (1966–1985, 1986–2005, 2006–2025, 2026–2045, 2046–2065, and 2066–2085) for the Canada Basin ($\approx$68–79°N, 124–160°W). (a) Annual mean surface ocean pH, (b) annual mean aragonite saturation state Ω_A, (c) maximum mixed layer depth Z_m (m) in March, and (d) sea ice concentration SIC in March (blue line) and September (red line) for RCP8.5. Shown are individual model averages (signs as per legend) as well as the multimodel mean (solid lines) and $\pm$1 standard deviation (black, blue, and red bars). Note that pH is not available for MIROC-ESM and Z_m is not available for MIROC-ESM and HadGEM2-ES.

3.3. Seasonal Variability in the Canada Basin

[15] To evaluate the impact of the seasonal cycle, monthly data for the surface properties (T, S, DIC, TA, Ω_A, and Ω_C) were examined for the Beaufort Sea/Canada Basin average (Figure 6). Temperature shows an increase in the amplitude of the seasonal cycle due to higher summer temperatures, with the largest increases for CanESM2 and IPSL-CM5A-LR (Figures 6a and 6b). These two models

Table 2. Multimodel-Averaged Bidecadal Means of Annual Mean pH, Z_m in March and Sea Ice Concentration in March and September, Averaged Over the Canada Basin ($\approx$70–78°N, 125–160°W) and Arctic Ocean (North of 64°N) Domains

Region	Variable	Scenario	1986–2005	2046–2065	2066–2085
Arctic Ocean	pH (annual mean)	hist/RCP4.5	8.12 ± 0.03	7.95 ± 0.03	7.92 ± 0.03
		hist/RCP8.5		7.89 ± 0.03	7.79 ± 0.02
	Z_m (m)	hist/RCP4.5	83.6 ± 17.7	77.3 ± 12.6	77.4 ± 12.6
		hist/RCP8.5		74.6 ± 12.8	71.9 ± 13.9
	SIC$_{Mar}$ (%)	hist/RCP4.5	87.4 ± 5.0	83.2 ± 5.5	81.9 ± 6.4
		hist/RCP8.5		81.7 ± 6.1	77.8 ± 8.2
	SIC$_{Sep}$ (%)	hist/RCP4.5	51.0 ± 10.7	18.5 ± 17.9	15.7 ± 17.9
		hist/RCP8.5		10.8 ± 12.4	3.6 ± 6.9
Canada Basin	pH[a] (annual mean)	hist/RCP4.5	8.12 ± 0.04	7.94 ± 0.03	7.9 ± 0.03
		hist/RCP8.5		7.87 ± 0.03	7.77 ± 0.03
	Z_m (m)	hist/RCP4.5	51.0 ± 9.7	48.8 ± 8.2	48.8.4 ± 4.7
		hist/RCP8.5		49.9 ± 8.2	48.8 ± 4.8
	SIC$_{Mar}$ (%)	hist/RCP4.5	96.5 ± 1.9	96.2 ± 2.1	96.1 ± 2.0
		hist/RCP8.5		95.6 ± 2.1	93.3 ± 5.1
	SIC$_{Sep}$ (%)	hist/RCP4.5	45.6 ± 14.0	11.8 ± 13.2	9.6 ± 9.7
		hist/RCP8.5		4.9 ± 6.8	0.4 ± 0.6

[a]Observed pH in surface waters in CARINA (1986–2005, mostly from July to September) and JOIS (2011) in the Canada Basin are: CARINA pH = 8.17 ± 0.09 (n = 1201), JOIS2011 pH = 8.06 ± 0.06 (n = 33), n being the number of measurements.

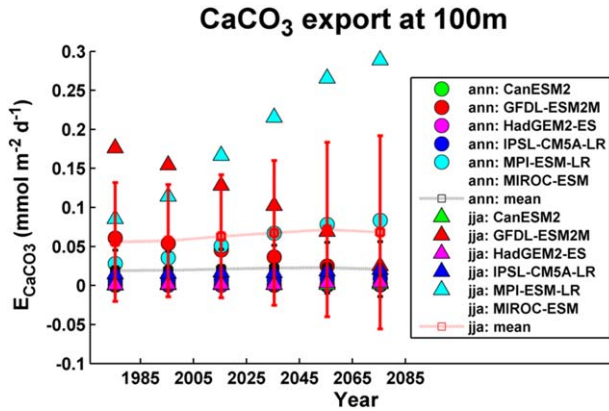**Figure 5.** Multimodel comparison of bidecadal averages for the Canada Basin of annual and summer (June, July, and August) mean downward flux of $CaCO_3$ at 100 m depth (mmol C m^{-2}d^{-1}). Shown are individual model averages (signs as per legend) as well as the multimodel mean (solid lines) and ± 1 standard deviation (red).

are at the low and the high end of the spectrum with respect to summer sea-ice cover, but simulate the shallowest mixed layers (Figures 4c and 4d), suggesting mixed layer depth as the main factor for surface temperature differences among the models. The multimodel mean seasonal range increases from 1.11°C in 1986–2005 to 6.16°C in 2066–2085. Over the same time period, multimodel mean salinities show a consistent freshening year round with a slight decrease in the seasonal amplitude from about 2.7 to 1.9 ppt, with a maximum in April and the minimum shifting from August to July. Intermodel differences are fairly constant over the year with up to 3 ppt between the freshest (HadGEM2-ES) and the saltiest model (GFDL-ESM2M) (not shown). CanESM2, which simulates the lowest summer ice cover (Figure 4d), shows a slightly larger seasonal range than the other models. The multimodel mean DIC also shows a decrease in the seasonal cycle from 0.19 mol m^{-3} in 1986–2005 to 0.14 mol m^{-3} in 2066–2085, again with a maximum in April and a minimum shifting from August to July. The decrease in seasonal range is caused by both a decrease in winter/spring and an increase in late summer by 2066–2085, although DIC decreases initially in summer. The variability in the summer DIC signal reflects the combined effects of dilution, biological uptake, and atmospheric CO_2 increase, which vary in their contribution over time. Intermodel differences change slightly with DIC decreasing more in winter for the models with reduced winter ice cover (e.g., CanESM2, HadGEM2-ES) and increasing less in summer for models with already reduced summer ice cover (CanESM2). In consequence, the models show a more consistent seasonal amplitude by 2066–2085 (Figures 6d–6f). The multimodel mean change in TA is dominated by dilution, leading to a continuous decrease over time, which is seen in all models (Figures 6g–6i). For 1986–2005, CanESM2 shows a pronounced minimum in TA in summer and an enhanced seasonal cycle compared to the other models. By 2066–2085, the CanESM2 amplitude of the seasonal cycle is more similar to the other models. Changes in the multimodel mean salinity-normalized TA (nTA) are very small and not consistent over time or season

(not shown). nTA increases through 2046–2065 for most of the year, and then decreases again. Simulated patterns for Ω_A and Ω_C are very similar and are only shown for Ω_A (Figures 6d–6f). The models show a consistent decrease in the multimodel mean from about 1.3 (2.09) to 0.74 (0.96) for the annual mean of Ω_A (Ω_C), and very little change in the seasonal amplitude, which ranges from 0.06 to 0.09 for Ω_A and 0.08 to 0.11 for Ω_C. The maximum occurs in June and shifts to August by 2066–2085, and the minimum shifts from October to November in 2026–2045 for both Ω_A and Ω_C.

[16] The saturation state is a nonlinear function of T, S, DIC, and TA, and the intermodel differences for both aragonite and calcite saturation state show influences of all of these drivers, but mainly of DIC and TA. The influences of the DIC and TA seasonal cycles on the seasonal cycle of Ω are both large but of opposite sign (i.e., DIC is diluted and drawn down by the biota in summer, driving Ω up, and TA is diluted, driving Ω down). The two effects largely offset each other, producing a relatively small seasonal amplitude change in Ω. The residual seasonal cycle is the sum of two large and opposite effects, so it is not surprising that the models differ in the timing and even the sign of the summer anomaly in Ω. The relative importance of the DIC and alkalinity effects varies among models, but in no case does either have a negligible effect. The increased summer temperature leads to an additional or extended maximum in Ω in August/September by 2066–2085 for most models.

3.4. Regional Variability in the Arctic

[17] Figure 7 (left) shows a regional view of the annual mean surface Ω_A in the Arctic as simulated at the end of the historical runs (1986–2005). Due to the coarse resolution of global ESMs, spatial variability is lower than observed, but for the recent past, Ω_A is between 1 and 1.4 in the CB for all models, within the range of observations [e.g., *Steinacher et al.*, 2009; *Yamamoto-Kawai et al.*, 2009]. The pattern close to the surface is influenced by temperature, Pacific water inflow through Bering Strait, open water areas and ice melt, river inflow and mixing on the shelves. All models except CanESM2 show Ω_A to be lowest on the Siberian Shelf, most notably in MPI-ESM-LR and MIROC-ESM (Figures 7i and 7j). Both of these models simulate somewhat reduced (90–95% compared to 100% in the other models) winter ice cover in this area (not shown), allowing for enhanced CO_2 uptake. This area is also characterized by shallow shelves and river inflow. The influence of the individual Arctic river input varies among the models, likely due to different distributions of river inflow over model grid cells. DIC and TA contributions are zero or biased low in all models. Excessive shelf depth in CanESM2 (190 m), which allows for deeper mixing in winter, might reduce the influence of river inflow at the surface and contribute to the higher saturation state in this area in CanESM2. However, summer ice cover in CanESM2 is already greatly reduced by 1986–2005, and limited to the area north of the CAA [*Steiner et al.*, 2013], which leads to enhanced stratification and a reduced saturation state in the central Arctic and CB, where CanESM2 simulates the lowest surface Ω_A (Figure 7e). The model with the highest surface Ω_A is GFDL-ESM2M (Figure 7b). Surface waters in the Eurasian Basin are influenced by Atlantic water inflow
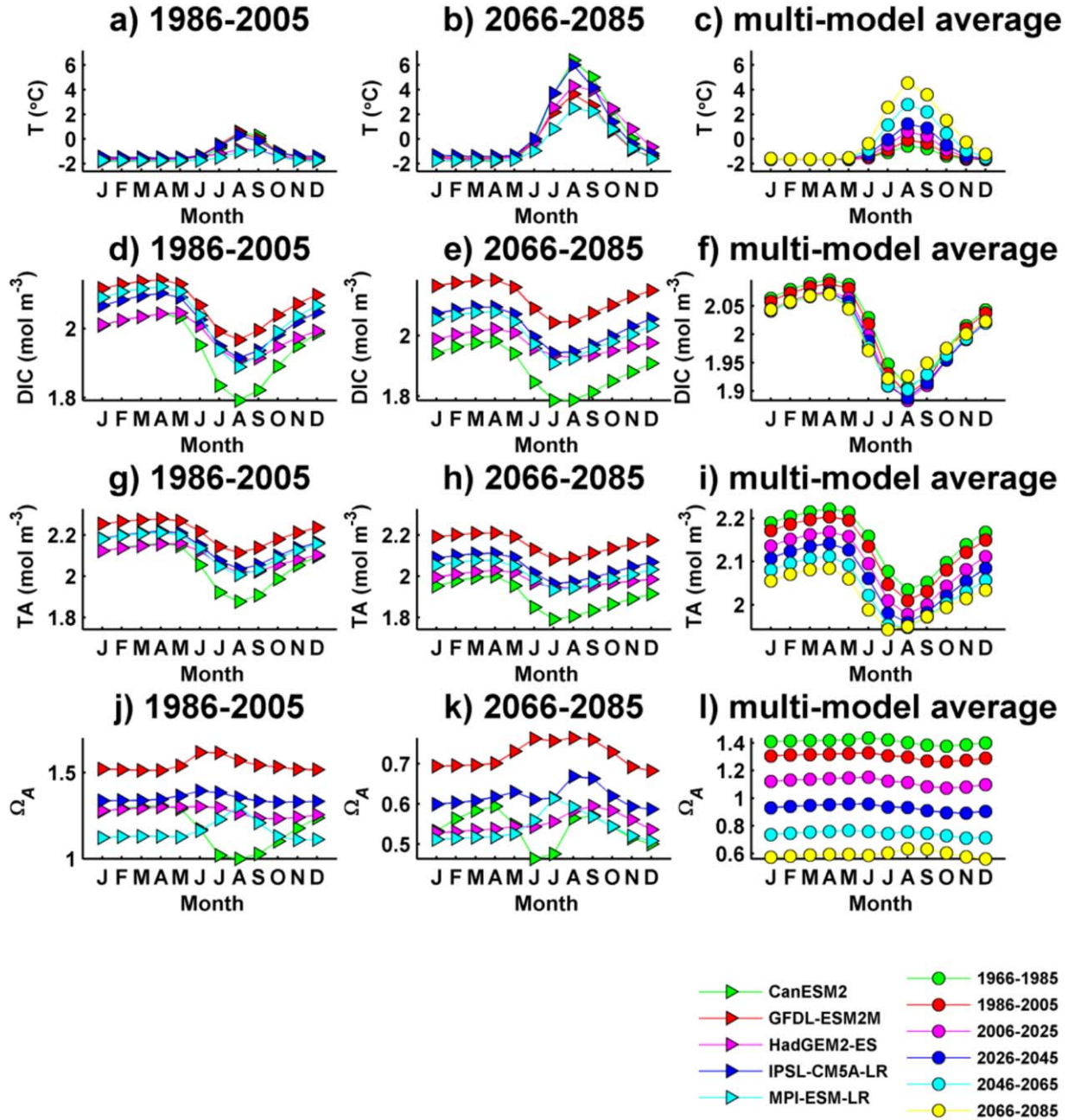
Figure 6. Simulated bidecadal mean seasonal cycles for the Canada Basin ($\approx$68–79°N, 124–160°W) for (a–c) temperature T (°C), (d–f) dissolved inorganic carbon DIC (mol m^{-3}), (g–i) total alkalinity TA (mol m^{-3}), and (j–l) aragonite saturation state Ω_A. Averages for 1986–2005 are shown on the left-hand side, 2066–2085 in the middle and multimodel mean averages from 1966–1985 to 2066–2085 are shown on the right-hand side.

and become undersaturated much later than the rest of the Arctic (Figure 7). For all models, Ω_C shows a similar pattern, but higher saturation states (1.7–2.4 for 1986–2005, not shown).

[18] Four of the models provide Z_m, allowing some estimate of mixing and stratification (Figure 8). Note that the color scale has been adjusted to optimally represent the features in the CB, hence areas with Z_m greater than 200 m and differences larger than ±50 m are shaded gray. Those areas give an indication of intermodel differences in the deep mixing in the northern North Atlantic which will affect the

inflow of Atlantic water into the Arctic Ocean. Highest Z_m in the CB area consistently occurs in March and reaches 60 m (CanESM2), 70 m (IPSL-CM5A-LR), 80 m (GFDL-ESM2M), and 100 m (MPI-ESM-LR) for the 1986–2005 time period with the spatial pattern, e.g., location of the deepest Z_m, slightly varying among the models. All models show a consistent future pattern, with shallower Z_m reaching about 60 m in the central CB for 2066–2085. This might point to a state indicative of sea ice free summers. March Z_m in this area remains slightly higher in GFDL-ESM2M, where localized summer ice concentrations above 50% still
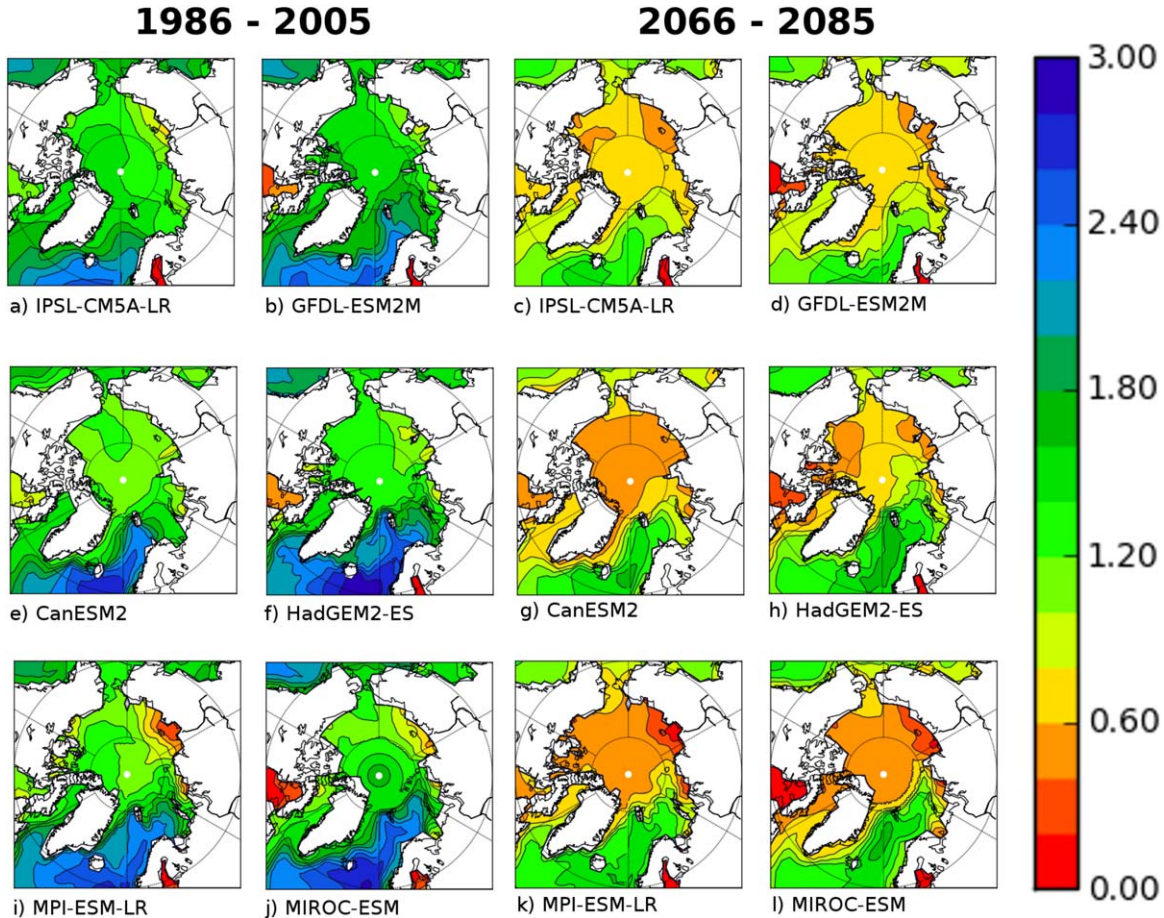
Figure 7. Surface aragonite saturation state Ω_A as simulated under the RCP8.5 scenario: (a, c) IPSL-CM5A-LR, (b, d) GFDL-ESM2M, (e, g) CanESM2, (f, h) HadGEM2-ES, (i, k) MPI-ESM-LR, (j, l) MIROC-ESM. 1986–2005 averages are shown in the two columns on the left-hand side and 2066–2085 on the right-hand side.

occur. CanESM2 shows the least change, corresponding to an already reduced sea-ice cover and shallower Z_m during the historical time period. Figure 8 (bottom) shows the difference in Z_m between 2066–2085 and 1986–2005, pointing out that the shallowing of Z_m is not universal across the Arctic, but limited mainly to the CB and the vicinity of the North Pole. Areas like the southern Beaufort Sea and other shelf areas show a deepening of Z_m, indicative of reduced stratification and enhanced mixing. The pattern of change in the coastal and shelf areas varies among the models. The different model representations of sea ice retreat, freshwater input, and atmospheric circulation affect both ice drift and ocean circulation, and likely contribute to the intermodel differences.

[19] In Figure 7 for the RCP8.5 projection runs, surface Ω_A reaches undersaturation in the entire Arctic region with the exception of the Barents Sea and North Atlantic. Surface Ω_A reaches its lowest values for MPI-ESM-LR, MIROC-ESM, and CanESM2, and shows a fairly consistent spatial pattern except that CanESM2 does not represent the reduced saturation state on the Siberian shelf. The highest surface saturation states are simulated in GFDL-ESM2M, in correspondence with largest retained summer ice cover in the CB as well as deepest Z_m. The saturation state around Greenland varies among models, likely in

response to simulated circulation patterns transporting undersaturated waters out of the Arctic.

[20] Figures 9 and 10 show the multimodel comparison of bidecadally averaged annual mean surface pH and Ω_A, Z_m in March, sea ice concentration in March and September for the domains of the Chukchi Sea (CS, ≈65–71°N, 162°W-170°E) and Baffin Bay (BB, ≈65–77°N, 60–78°W). Again the consistency in the projected decrease in pH is apparent. Ω_A shows a corresponding decrease, although intermodel differences are somewhat larger especially in BB. Z_m in BB shows a consistent decrease over time; however, Z_m increases in the CS. The latter also shows larger intermodel variability as. While no major sea ice decline is visible in Figures 9 and 10, this is mainly because summer sea ice cover is generally low in these areas, but the ice cover does in fact decrease from about 8% to 1% in BB and from about 10% to zero in the CS. In BB and CS, the winter ice cover shows some decrease as well, from 90% to 87% (BB) and 92% to 84% (CS) (changes are from 1986–2005 to 2066–2085).

3.5. The Aragonite Saturation Horizon

[21] CMIP5 multimodel time series of the zonal mean saturation horizon (the layer where $\Omega = 1.0$) show a continuous shoaling from preindustrial times to 2100 over most
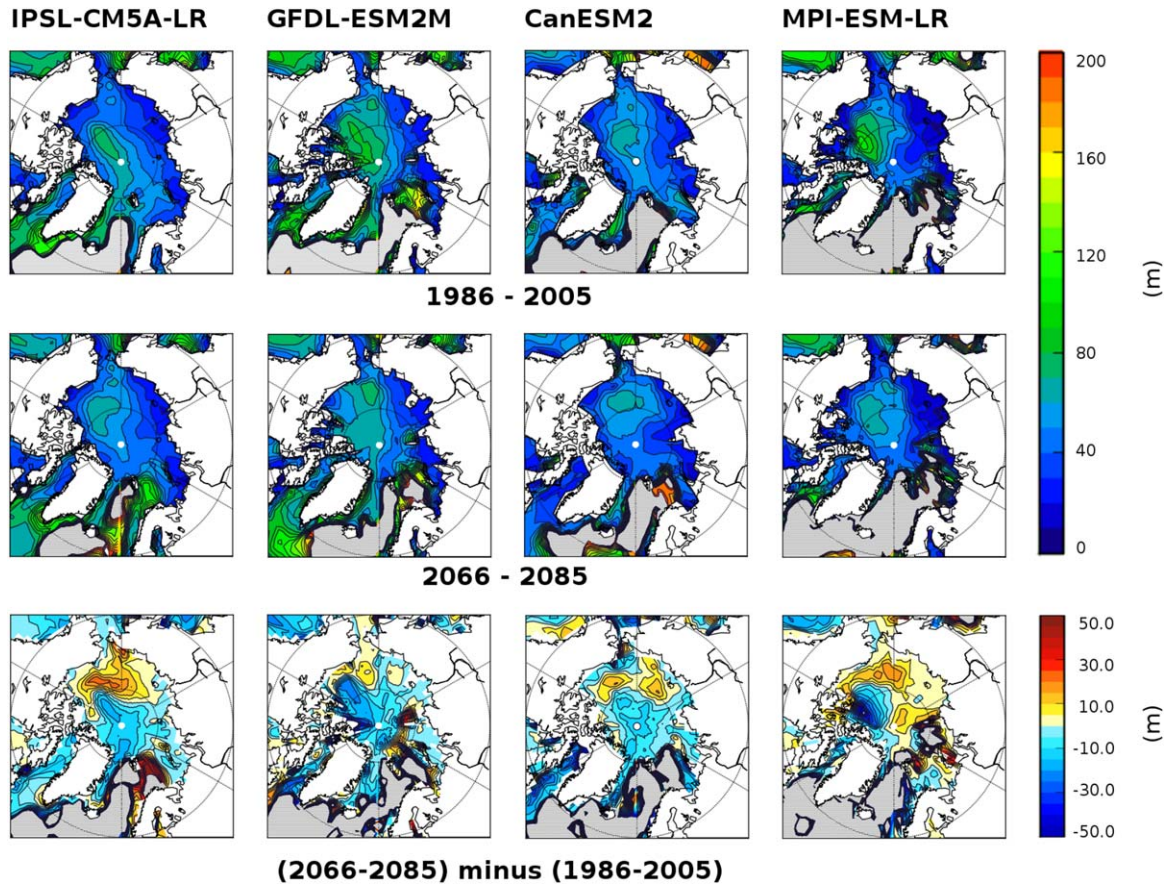
Figure 8. Bidecadal averages of simulated maximum mixed layer depth (Z_m) in March (m) for the IPSL-CM5A-LR, GFDL-ESM2M, CanESM2, and MPI-ESM-LR models for the RCP8.5 scenario. (top) 1986–2005 averages and (middle) 2066–2085. (bottom) Differences between future projections and recent past ((2066–2085) − (1986–2005)). Note that the color scale has been adjusted to optimally represent the features in the CB, hence areas with Z_m greater than 200 m and differences larger than ± 50 m are shaded gray and give an indication of intermodel differences in the deep mixing in the northern North Atlantic.

latitude bands (not shown). For the Arctic, however, in addition to a deep saturation horizon, a shallow saturation horizon starts to form close to the surface in the near future. This feature is consistent in all models and is also seen in the NCAR CSM1.4 carbon simulations for the SRES scenario A2 presented in *Steinacher et al.* [2009]. Table 1 lists the timing of the occurrence of undersaturation in the annual mean at the surface, indicating the appearance of the shallow saturation horizon at a representative location in the central CB (75°N, 140°W). For most models, undersaturation at the surface occurs within the next decade: For HadGEM2-ES, MIROC-ESM, and MPI-ESM-LR, surface undersaturation occurs around 2015, for CanESM2 in 2020, and for GFDL-ESM2M and IPSL-CM5A-LR around 2040. Since the two scenarios RCP 4.5 and 8.5 do not begin to diverge until 2006, differences in the 2010s and 2020s between them are very small. Figure 11 shows the time series of Ω_A from the surface to about 3500 m at this location for RCP8.5. Affected by ice melt and inflow of Pacific water with a naturally low saturation state, near surface ocean waters become undersaturated first and undersaturated layers expand from the top and the bottom, essentially forming a shallow (in the observations and some model

representations there are two shallow undersaturated layers at the surface and subsurface) and a deep saturation horizon. The depth at which the shallow undersaturated layer and the intermediate supersaturated water are separated initially remains close to the surface, then increases to ~100 m, where it temporarily stagnates (consistently for most models), and deepens to about 300 m by 2100. The deep saturation horizon varies between about 2000 and 4000 m among models, and the models show large differences in the saturation state of the ocean interior. It is not clear at this point if these differences are linked to different circulation patterns or biogeochemical parameterizations.

4. Discussion

[22] The lack of crucial baseline biogeochemistry data in the Arctic has been pointed out in recent reviews by *Wassmann et al.* [2011] and *Carmack and McLaughlin* [2011]. No gridded data sets of carbon chemistry are available for the Arctic, hence comparison with observations is limited to temporal and spatial snapshots obtained from irregular research cruises and limited term programs, e.g., the Canadian Arctic Shelf Exchange Study (CASES), the Joint
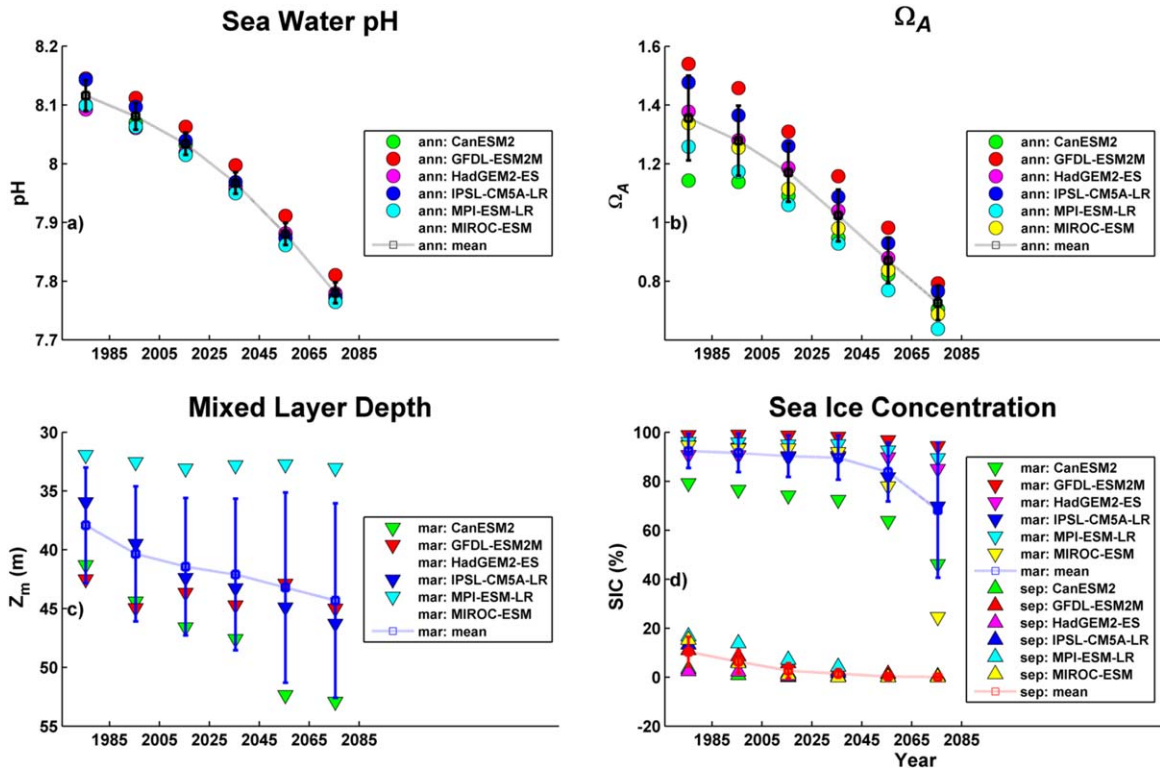
Figure 9. As Figure 4 for the Chukchi Sea ($\approx$65–71°N, 162°W–170°E).
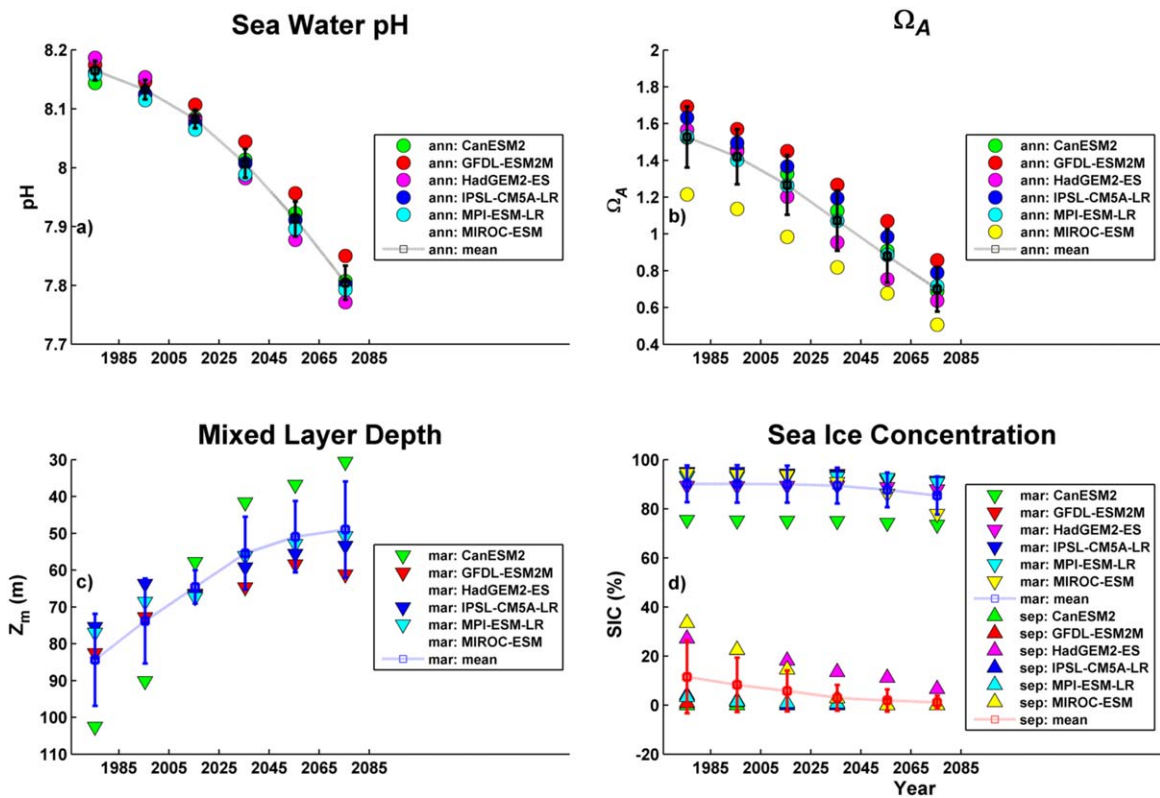
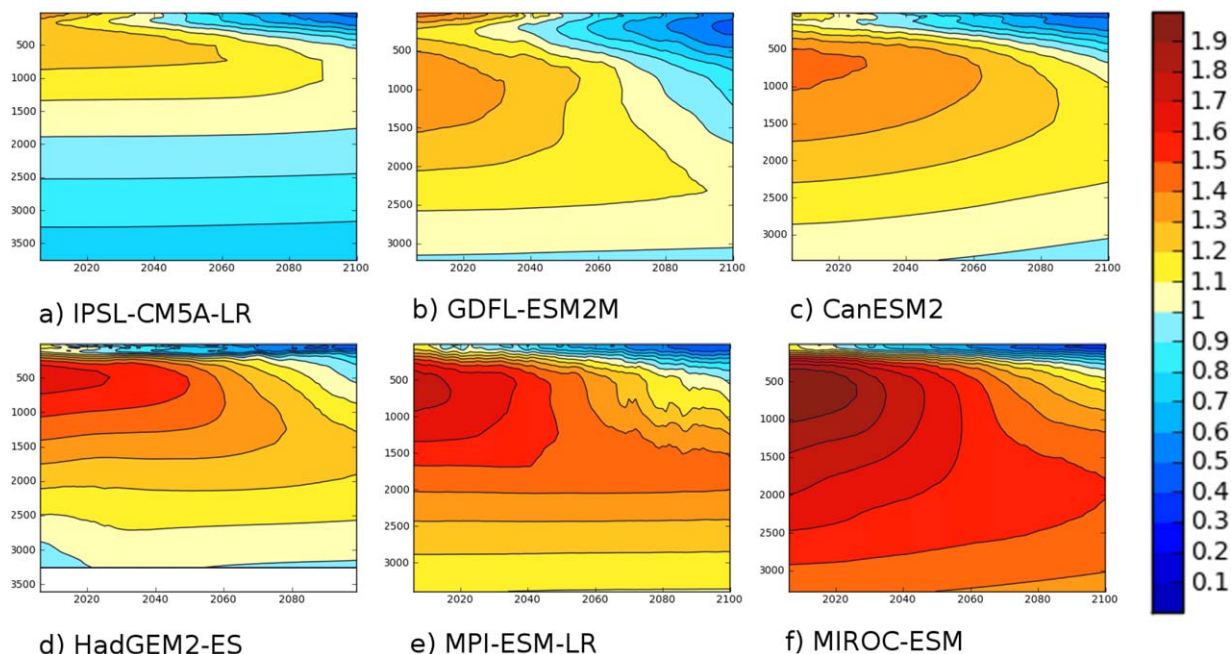**Figure 10.** As Figure 4 for Baffin Bay ($\approx$65–77°N, 60–78°W).

Figure 11. Time series of aragonite saturation state Ω_A in the deepest section of the central Canada Basin (77.5°N, 136°W) as simulated for the RCP8.5 scenario: (a) IPSL-CM5A-LR, (b) GFDL-ESM2M, (c) CanESM2, (d) HadGEM2-ES, (e) MPI-ESM-LR, and (f) MIROC-ESM. Vertical axis shows depth in meters and horizontal axis shows time in years.

Ocean Ice Study (JOIS) and the Canada's 3 Oceans program [e.g., *Carmack et al.*, 2012]. This scarcity of observations severely limits our ability to validate ESM results for historical and current time periods. ESMs are not designed to reproduce individual snapshots, but rather to represent changes on decadal timescales. Hence, the comparison between individual observation-based temporal and spatial snapshots and simulated decadal or bidecadal averages representing areas in excess of 100 km^2 is rather inadequate. It is not surprising that large differences exist between the individual models in the representation of the carbon system variables DIC and TA, and to a certain extent even S and T, and consequently the simulated pH and Ω. Similar issues have been pointed out with respect to ESM representations of nutrients and primary production in the Arctic [*Vancoppenolle et al.*, 2013].

[23] The connection between sea ice retreat and surface acidification is strong: increased open water areas allow for enhanced CO_2 uptake and freshwater contributions due to ice melt cause additional uptake. The relationship between acidification and mixing is less straightforward. Retreating sea ice exposes larger areas of open water allowing enhanced transfer of wind energy from the atmosphere into the ocean, which can cause deeper mixing and/or upwelling, e.g., over suddenly exposed shelf breaks. On the other hand, the accumulation of freshwater in the near surface ocean causes a more stable haline stratification, which can suppress mixing and limit the CO_2 uptake capacity [*Cai et al.*, 2010; *Steiner et al.*, 2013]. The models show that in the deep Canada Basin the stabilization dominates. For models with seaice free summers, a connection between increased acidification and enhanced stratification can be explained by the fact that CO_2 exchange is limited to a

smaller volume of water. However, due to the models' differences in vertical structure, deeper mixing allows entrainment of less saturated waters into the surface layer in some models and entrainment of more saturated waters in others. Hence, the response to enhanced stratification is uncertain. The pattern of Z_m change in coastal and shelf areas is not uniform among models; in areas with enhanced mixing and shelf break upwelling the origin of the upwelled water masses will again determine if the saturation state increases or decreases. The discrepancy in the projected Z_m change in the coastal and shelf areas compared with some of the deep ocean basins is likely caused by the combined effects of sea ice retreat, freshwater input, and simulated atmospheric circulation patterns affecting both ice drift and ocean circulation. Model bathymetry may be an additional contributing factor, e.g., by affecting mixing on the shelves and near the shelf break. Nonetheless the analysis suggests that the pace of the surface ocean acidification is not only related to the rate of sea ice reduction [*Yamamoto et al.*, 2012] but also linked to the related responses of wind mixing and stratification.

[24] We have been unable to clearly link differences in simulated Arctic saturation states to the representation of biochemical processes in the models. No clear relationship to simulated ecosystem complexity can be seen. The representation of calcification in the models, which removes alkalinity at the surface and increases alkalinity in the subsurface, can explain the difference between GFDL-ESM2M and MPI-ESM-LR in the upper 150 m, but does not explain the larger intermodel differences.

[25] At this point, all models simulate rain ratios that decline at high latitudes, with values close to zero in the Arctic for all models except MPI-ESM-LR and GFDL-ESM2M.

These parameterizations are based in part on the analysis of *Sarmiento et al.* [2002], which showed the highest rain ratios in the tropics, decreasing toward the poles. However, their study did not include the Arctic, and they expressed limited confidence with respect to the latitudinal distribution. Particle flux measurements by *Honjo et al.* [2010] in the Canada Basin show rain ratios not very different from Sarmiento et al.'s estimated global mean of 0.06. However, organic carbon fluxes are much more variable than inorganic carbon fluxes, so that rain ratios range from <0.01, to as much as 0.29 under conditions of extremely low organic flux. *Honjo et al.* [2010] indicate potentially large regional differences, e.g., in shelf areas versus the deep Canada Basin. This is consistent with *Charalampopoulou et al.* [2011] who found extremely low rates of pelagic calcification at several Arctic stations, but values up to two orders of magnitude higher at a high-latitude station in the Norwegian Basin. There is some evidence to support the idea that calcification in polar waters is limited [e.g., *Winter et al.*, 1994; *Charalampopoulou*, 2011], but the assumption of uniformly negligible rates is probably not warranted [*Honjo et al.*, 2010].

[26] The seasonal amplitude in Ω is remarkably unaffected in future projections, the reason being that the seasonally enhanced sea ice melt cycle affects both DIC and TA strongly (dilution in summer), but these have opposite effects on Ω which largely cancel each other out. However, other effects which might effect the seasonal cycle of DIC and TA differently might not be included, e.g., river inflow. A recent evaluation of DIC flux from rivers into the Arctic by *Tank et al.* [2012] estimated the DIC flux in the Arctic to be 13–15% of the total global flux. They found considerable and synchronous, seasonal variations across the analyzed rivers. At this point in time none of the ESMs includes seasonal varying DIC or TA entries from rivers, DIC and TA contributions are zero or biased low.

[27] Some of the simulated differences may also be related to different landmasks, e.g., opening of channels and passages affecting in, out and through flows (see Table 1). However, a clear relationship between the saturation state in the central Arctic and, e.g., the presence of passages through the CAA cannot be found. We suggest that at this point physical model differences affecting wind patterns, sea ice melt and resulting open water areas, wind mixing and salinity stratification still dominate the intermodel differences with respect to the ocean carbon system.

5. Summary

[28] Six ESMs that are contributing results to CMIP5 have been analyzed and compared with respect to Arctic Ocean acidification, and specifically the $CaCO_3$ saturation state in the Canada Basin. The study provides a preview suggesting continued Arctic Ocean acidification over the next century with accelerated reductions in calcium carbonate saturation state at least until the sea ice cover reaches a new steady state with largely ice free summers. Three main limitations affect ESM projections of the ocean carbon system. First, long-term observations of the Arctic Ocean carbon system are sparse and for many locations nonexistent. This significantly affects our ability to constrain the models, which show large differences in carbon system variables. Second, horizontal and vertical model resolution in

ESMs is still limiting, affecting basin exchange and throughflow as well as mixing processes on shelves which can cause misrepresentation and differences between models. Third, sea ice retreat varies markedly between models, causing uncertainties in the timing and location of calcium carbonate undersaturation.

[29] Despite these limitations, some consensus emerges and strengthens earlier results: The reduction in pH and calcium carbonate saturation state over the 21st century is a robust signal, despite a large model spread in September sea-ice cover. The pH in the Canada Basin decreases from about 8.1 in the recent past to about 7.7 by the end of the century, with a reduction in the saturation state of mineral calcium carbonate from about 1.2 (2.0) to about 0.6 (1.0) for aragonite (calcite) for RCP8.5. The seasonal amplitude shows little change, since the main drivers (dilution of DIC and TA) have opposite effects on the saturation state. An emission scenario with mitigation (RCP4.5) reduces the progress of undersaturation (pH of 7.9 is reached about 25 years later in RCP4.5 than in RCP8.5). However, the emergence of undersaturated surface waters, which is projected to occur within the next decade differs little between the scenarios, which are very similar for the first few decades after 2005. The models indicate a strong connection between simulated acidification and sea ice reduction but also indicate links to stratification, as represented by maximum mixed layer depth. Maximum mixed layer depths decline from 80–100 m to $\approx$60 m in the central Canada Basin under seasonally ice free conditions, but increase in several coastal areas and shelf seas, e.g., the Chukchi Sea.

[30] The Canada Basin shows a characteristic layering with respect to saturation states. Affected by ice melt and inflowing Pacific water, two shallow undersaturated layers form at the surface and subsurface creating a shallow saturation horizon which expands from the surface downward. This is in addition to the globally observed deep saturation horizon which is continuously expanding upward with increasing CO_2 uptake. Surface waters in the Eurasian Basin become undersaturated much later than in the rest of the Arctic.

[31] The influence of rivers is not well represented at this point. River inflows of DIC and TA are lacking or underestimated in ESMs and do not represent the observed seasonal or spatial variability. Similarly the potential separation of DIC and TA during sea-ice freezing is neglected. The impact of fluvial sources of DIC and TA needs to be examined in order to evaluate the requirement for proper representation in the next generation of ESMs.

[32] We conclude that ESM projections provide a first glimpse of future Arctic Ocean acidification, but higher-resolution regional models of the Arctic marine ecosystem are needed to identify, analyze and understand local changes and impacts. Also, the lack of observational data is apparent; more consistent and expanded observations of the marine carbon system are urgently needed to validate the model outcomes for current times and reduce uncertainty in future projections.

References

AMAP (2013), AMAP Arctic ocean acidification assessment: Summary for policy-makers, technical report, 12 pp., Arctic Monit. and Assess. Programme, Oslo, Norway.

Arora, V., J. Scinocca, G. Boer, J. Christian, K. Denman, G. Flato, V. Kharin, W. Lee, and W. Merryfield. (2011), Carbon emission limits required to satisfy future representative concentration pathways of greenhouse gases, *Geophys. Res. Lett.*, *38*, L05805, doi:10.1029/2010GL046270.

Aumont, O., E. Maier-Reimer, S. Blain, and P. Monfray (2003), An ecosystem model of the global ocean including Fe, Si, P colimitations, *Global Biogeochem. Cycles*, *17*(2), 1060, doi:10.1029/2001GB001745.

Bates, N., and J. Mathis (2009), The Arctic ocean marine carbon cycle: Evaluation of air-sea CO_2 exchanges, ocean acidification impacts and potential feedbacks, *Biogeosciences*, *6*, 2433–2459.

Bracegirdle, T., and D. Stephenson (2013), On the robustness of emergent constraints used in multimodel climate change projections of arctic warming, *J. Clim.*, *26*, 669–678, doi:10.1175/JCLI-D-12-00537.1.

Cai, W.-J., et al. (2010), Decrease in the CO_2 uptake capacity in an ice-free Arctic ocean basin, *Science*, *329*(5991), 556–559, doi:10.1126/science.1189338.

Carmack, E., and F. McLaughlin (2011), Towards recognition of physical and geochemical change in subarctic and Arctic seas, *Prog. Oceanogr.*, *90*, 90–104.

Carmack, E. C., F. A. McLaughlin, S. Vagle, H. Melling, and W. J. Williams (2012), Structures and property distributions in the three oceans surrounding Canada in 2007: A basis for a long-term ocean climate monitoring strategy, *Atmos. Ocean*, *48*(4), 211–224, doi:10.3137/OC324.2010.

Charalampopoulou, A. (2011), Coccolithophores in high latitude and polar regions: Relationships between community composition, calcification, and environmental factors, PhD thesis, Univ. of Southampton, Southampton, U. K.

Charalampopoulou, A., A. Poulton, T. Tyrrell, and M. Lucas (2011), Irradiance and ph affect coccolithophore community composition on a transect between the North Sea and the Arctic Ocean, *Mar. Ecol. Prog. Ser.*, *431*, 25–43, doi:10.3354/meps09140.

Chierici, M., and A. Fransson (2009), Calcium carbonate saturation in the surface water of the Arctic Ocean: Undersaturation in freshwater influenced shelves, *Biogeosciences*, *6*(11), 2421–2431.

Christian, J., et al. (2010), The global carbon cycle in the Canadian Earth System Model (CanESM1): Preindustrial control simulation, *J. Geophys. Res.*, *115*, G03014, doi:10.1029/2008JG000920.

Collins, W., et al. (2011), Development and evaluation of an earth-system model: HadGEM2, *Geosci. Model Dev.*, *4*(4), 1051–1075, doi:10.5194/gmd-4-1051-2011.

Deal, C., et al. (2013), Progress and challenges in biogeochemical modeling of the Pacific Arctic region, in *The Pacific Arctic Region: Ecosystem Status and Trends in a Rapidly Changing Environment*, Springer, in press.

Denman, K., et al. (2007), Couplings between changes in the climate system and biogeochemistry, in *Contribution of Working Group I to the Fourth Assessment Report of the Intergovernmental Panel on Climate Change*, Cambridge Univ. Press, New York.

Denman, K., J. Christian, N. Steiner, H.-O. Pörtner, and Y. Nojiri (2011), Potential impacts of future ocean acidification on marine ecosystems and fisheries, *ICES J. Mar. Sci.*, *68*(6), 1019–1029, doi:10.1093/icesjms/fsr074.

Dickson, A., C. Sabine, and J. Christian (2007), *Guide to Best Practices for Ocean CO_2 Measurements*, vol. 3, 191 pp., PICES Spec. Publ., North Pacific Marine Science Organisation, Sidney, Canada.

Dufresne, J.-L., et al. (2013), Climate change projections using the IPSL-CM5 earth system model: From CMIP3 to CMIP5, *Clim. Dyn.*, *40*, 2123–2165, doi:10.1007/s00382-012-1636-1.

Dunne, J., et al. (2012), GFDL's ESM2 global coupled climate-carbon earth system models. Part I: Physical formulation and baseline simulation characteristics, *J. Clim.*, *25*(19), 6646–6665.

Dunne, J., et al. (2013), GFDL's ESM2 global coupled climate-carbon earth system models. Part II: Carbon system formulation and baseline simulation characteristics, *J. Clim.*, *26*(7), 2247–2267, doi:10.1175/JCLI-D-12-00150.1.

Friedlingstein, P., et al. (2006), Climate-carbon cycle feedback analysis: Results from the C4MIP model intercomparison, *J. Clim.*, *19*, 3337–3353, doi:10.1175/JCLI3800.1.

Gattuso, J.-P., and L. Hansson (Eds.) (2011), *Ocean Acidification*, Oxford Univ. Press, New York.

Giorgetta, M., et al. (2013), Climate and carbon cycle changes from 1850 to 2100 in MPI-ESM simulations for the coupled model intercomparison project phase 5, *J. Adv. Model. Earth Syst.*, *5*, 572–597.

HadGEM2 Development Team (2011), The HadGEM2 family of met office unified model climate configurations, *Geosci. Model Dev.*, *4*(3), 723–757, doi:10.5194/gmd-4-723-2011.

Hauck, J., M. Hoppema, R. Bellerby, C. Völker, and D. Wolf-Gladrow (2010), Data-based estimation of anthropogenic carbon and acidification in the Weddell Sea on a decadal timescale, *J. Geophys. Res.*, *115*, C03004, doi:10.1029/2009JC005479.

Honjo, S., R. Krishfield, T. Eglinton, S. Manganini, J. Kemp, K. Doherty, J. Hwang, T. McKee, and T. Takizawa (2010), Biological pump processes in the cryopelagic and hemipelagic arctic ocean: Canada Basin and Chukchi Rise, *Prog. Oceanogr*, *85*, 137–170.

Ilyina, T., K. D. Six, J. Segschneider, E. Maier-Reimer, H. Li, and I. Nunez-Riboni (2013), The global ocean biogeochemistry model HAMOCC: Model architecture and performance as component of the MPI-Earth System Model in different CMIP5 experimental realizations, *J. Adv. Model. Earth Syst.*, *5*, 287–315, doi:10.1002/jame.20017.

Kawamiya, M., M. J. Kishi, and N. Suginohara (2000), An ecosystem model for the North Pacific embedded in a general circulation model: Part I: Model description and characteristics of spatial distributions of biological variables, *J. Mar. Syst.*, *25*, 129–157.

Loose, B., W. R. McGillis, P. Schlosser, D. Perovich, and T. Takahashi (2009), Effects of freezing, growth, and ice cover on gas transport processes in laboratory seawater experiments, *Geophys. Res. Lett.*, *36*, L05603, doi:10.1029/2008GL036318.

Lueker, T., A. Dickson, and C. D. Keeling (2000), Ocean pCO_2 calculated from dissolved inorganic carbon, alkalinity, and equations for K1 and K2: Validation based on laboratory measurements of CO_2 in gas and seawater at equilibrium, *Mar. Chem.*, *70*, 105–119.

Maslowski, W., J. C. Kinney, M. Higgins, and A. Roberts (2012), The future of Arctic sea ice, *Annu. Rev. Earth Planet. Sci.*, *40*, 625–654, doi:10.1146/annurev-earth-042711-105345.

Millero, F. J. (1979), Thermodynamics of the carbon dioxide system in the oceans, *Geochim. Cosmochim. Acta*, *59*, 661–677.

Moss, R. H., et al. (2010), The next generation of scenarios for climate change research and assessment, *Nature*, *463*, 747–756, doi:10.1038/nature08823.

Mucci, A. (1983), The solubility of calcite and aragonite in seawater at various salinities, temperatures, and one atmosphere total pressure, *Am. J. Sci.*, *283*, 780–799.

Nakicenovic, G., et al. (2000), IPCC special report on emissions scenarios, technical report, Cambridge Univ. Press, New York.

Orr, J., et al. (2005), Anthropogenic ocean acidification over the twenty-first century and its impacts on calcifying organisms, *Nature*, *437*, 681–686.

Sarmiento, J., J. Dunne, A. Gnanadesikan, R. M. Key, K. Matsumoto, and R. Slater (2002), A new estimate of the $CaCO_3$ to organic carbon export ratio, *Global Biogeochem. Cycles*, *16*(4), 1107, doi:10.1029/2002GB001919.

Schneider, B., L. Bopp, M. Gehlen, J. Segschneider, T. L. Frölicher, P. Cadule, P. Friedlingstein, S. C. Doney, M. J. Behrenfeld, and F. Joos (2008), Climate-induced interannual variability of marine primary and export production in three global coupled climate carbon cycle models, *Biogeosciences*, *5*, 597–614.

Steinacher, M., F. Joos, T. Frölicher, G.-K. Plattner, and S. Doney (2009), Imminent ocean acidification of the Arctic projected with the NCAR global coupled carbon-cycle climate model, *Biogeosciences*, *6*(4), 515–533.

Steinacher, M., et al. (2010), Projected 21st century decrease in marine productivity: A multi-model analysis, *Biogeosciences*, *7*, 979–1005.

Steiner, N. S., W. G. Lee, and J. R. Christian (2013), Enhanced gas fluxes in small sea ice leads and cracks: Effects on CO_2 exchange and ocean acidification, *J. Geophys. Res. Oceans*, *118*, 1195–1205, doi:10.1002/jgrc.20100.

Stroeve, J., M. Serreze, F. Fetterer, T. Arbetter, W. Meier, J. Maslanik, and K. Knowles (2005), Tracking the Arctic's shrinking ice cover: Another extreme September minimum in 2004, *Geophys. Res. Lett.*, *32*, L04501, doi:10.1029/2004GL021810.

Stroeve, J. C., V. Kattsov, A. Barrett, M. Serreze, T. Pavlova, M. Holland, and W. N. Meier (2012), Trends in Arctic sea ice extent from CMIP5, CMIP3 and observations, *Geophys. Res. Lett.*, *39*, L16502, doi:10.1029/2012GL052676.

Tank, S. E., P. Raymond, R. G. Striegl, J. W. McCleland, R. M. Holmes, G. J. Fiske, and B. J. Peterson (2012), A land-to-ocean perspective on the magnitude, source and implication of DIC flux from major Arctic rivers to the Arctic Ocean, *Global Biogeochem. Cycles*, *26*, GB4018, doi:10.1029/2011GB004192.

Taylor, K. E., R. J. Stouffer, and G. A. Meehl (2012), An overview of CMIP5 and the experiment design, *Bull. Am. Meteorol. Soc.*, *93*, 485–498, doi:10.1175/BAMS-D-11-00094.1.

Vancoppenolle, M., L. Bopp, C. Madec, J. Dunne, T. Ilyina, P. Halloran, and N. Steiner (2013), Future Arctic primary productivity from CMIP5 simulations: Uncertain outcome, but consistent mechanisms, *Global Biogeochem. Cycles*, *27*, 605–619, doi:10.1002/gbc.20055.

Wassmann, P., C. M. Duarte, S. Agusti, and M. K. Sejr (2011), Footprints of climate change in the Arctic marine ecosystem, *Global Change Biol.*, *17*, 1235–1249, doi:10.1111/j.1365-2486.2010.02311.

Watanabe, S., et al. (2011), MIROC-ESM 2010: Model description and basic results of CMIP5–20c3m experiments, *Geosci. Model Dev.*, *4*(4), 845–872, doi:10.5194/gmd-4-845-2011.

Winter, A., R. Jordan, and P. Roth (1994), Biogeography of living coccolithophores in ocean waters, in *Coccolithophores*, pp. 161–177, Cambridge Univ. Press, Cambridge, U. K.

Yamamoto, A., M. Kawamiya, A. Ishida, Y. Yamanaka, and S. Watanabe (2012), Impact of rapid sea-ice reduction in the Arctic ocean on the rate of ocean acidification, *Biogeosciences*, *9*, 2365–2375, doi:10.5194/bg-9-2365-2012.

Yamamoto-Kawai, M., F. McLaughlin, E. Carmack, S. Nishino, and K. Shimada (2009), Aragonite undersaturation in the Arctic ocean: Effects of ocean acidification and sea ice melt, *Science*, *326*(5956), 1098–1100.

Yamamoto-Kawai, M., F. McLaughlin, and E. Carmack (2011), Effects of ocean acidification, warming and melting of sea ice on aragonite saturation of the Canada Basin surface water, *Geophys. Res. Lett.*, *38*, L03601, doi:10.1029/2010GL045501.